A Digital Beamforming Fast-Start Passive Radar for Indoor Motion Detection and Angle Estimation

Aaron B. Carman, *Graduate Student Member, IEEE*, and Changzhi Li, *Fellow, IEEE*

***Abstract*— As wireless sensing and communications technologies continue to advance, the limited bandwidth in the microwave and millimeter-wave spectra has sparked new research in improved spectrum efficiency. Microwave radar sensors have seen considerable use as a noncontact sensor but contribute to spectrum congestion when many radar sensors are placed in one environment. Furthermore, traditional radar sensors pose security concerns since their illumination signals can be detected or spoofed. Passive sensing has demonstrated the potential to detect millimeter-scale (mm-scale) motions using ambient signals, but recent works have so far been limited to one- or two-channel systems incapable of determining the angle of a target with sufficient resolution. In addition, noise and clutter effects on passive sensing and beamforming models have not yet been considered, which creates performance limitations in passive sensing when no signals originate onboard. This article proposes a passive radar beamforming architecture that can sense and simultaneously determine a target's angle using 16 digital beamforming channels and a third-party microwave transmitter. The proposed architecture leverages a custom radio frequency front end to downconvert received signals to a baseband and a fast-startup baseband amplifier to allow for rapid measurements of low-frequency signals after powering the radar. The theory of passive radar beamforming is provided along with noise and clutter models to model the performance of beamforming passive sensing systems more accurately. The design procedure for the radio frequency front end and beamforming array are provided to ensure adequate performance of the final array. The experimental results show that the radar is capable of accurately measuring the angle of a cooperative transmitter in a controlled environment, as well as the respiration frequency and angle of a human target.**

***Index Terms*— Beamforming radar, Doppler passive radar, passive radar design, passive sensing, radar, receiver, RF front end.**

I. Introduction

MICROWAVE radar sensing uses the phase delay and Doppler frequency shift of traveling electromagnetic (EM) waves to detect target parameters such as distance and motion wirelessly [1]. Many radars that are used today leverage active radar architectures, meaning that the sensor transmits a dedicated signal to illuminate a target and compares the reflected waves to the known reference. Based on these architectures, microwave radar has been used in many applications such as vital-sign detection [2], [3], [4], gesture recognition [5], automotive sensing [6], [7], [8], and smart-infrastructure technologies [9], [10]. Furthermore, as the Internet of Things (IoT), autonomous vehicles, and smart healthcare technologies continue to advance, the number of deployed radar sensors continues increasing to address a variety of applications in day-to-day life [11]. As a result, active radar can experience difficulties when scaling due to interference issues among sensors within the same area. This becomes especially true as the EM spectrum becomes more congested, and engineers begin focusing on advanced techniques to share and minimize spectrum usage. In addition, active radar systems can create security concerns since the radar's illumination signal can be detected and spoofed to confuse the radar sensor [12].

Passive radar sensing, on the other hand, leverages ambient EM waves to accomplish target detection [13]. As a result, interference issues can be removed entirely while conserving power and cost due to the lack of transmitters in passive sensors. Traditionally, passive radars relied upon large, high-power illuminators of opportunity such as digital-audio [14] or digital-video broadcast [15], [16] towers to detect the distance of targets with multichannel receivers to isolate the reference and surveillance signals. Enabled by trends in software-defined radio and the proliferation of ubiquitous wireless signals, however, recent years have seen considerable interest in using passive radar for close-range sensing. Existing techniques for passive radar sensing can be broken down into two primary approaches: software- and hardware-enabled.

Software-enabled approaches leverage the capabilities of modern transceivers such as Wi-Fi access points or software-defined radios to measure the motions and positions of targets. Some approaches leverage the Wi-Fi protocol's signal metrics including channel state information (CSI) [17], [18] and received signal strength (RSS) [19], [20] to monitor small motions indoors for applications such

Manuscript received 15 February 2024; revised 10 April 2024; accepted 14 April 2024. This work was supported by the National Science Foundation (NSF) under Grant ECCS-2030094. This article is an expanded version from the IEEE Radio & Wireless Week, San Antonio, TX, USA, January 21–25, 2024 [DOI: 10.1109/WiSNeT59910.2024.10438569]. *(Corresponding author: Aaron B. Carman.)*

The authors are with the Department of Electrical and Computer Engineering, Texas Tech University, Lubbock, TX 79409 USA (e-mail: aaron.b.carman@ttu.edu; changzhi.li@ttu.edu).

Color versions of one or more figures in this article are available at https://doi.org/10.1109/TMTT.2024.3391062.

Digital Object Identifier 10.1109/TMTT.2024.3391062

as sleep studies [21]. Furthermore, Wi-Fi has been used to localize targets with centimeter-level precision by using a broad bandwidth and multiple access points [22], [23]. Other approaches have leveraged software-defined receivers to detect targets using advanced Wi-Fi signal processing in several applications including automotive [24], [25], human and drone localization [26], [27], and home healthcare [28], [29], [30], [31]. Reference-free approaches have been used to detect motions without a known reference [32], [33]. Beamforming techniques have also been used to provide angular information [34]. These approaches, however, rely heavily on commercial Wi-Fi transceivers or signal demodulation to extract target metrics, increasing cost and size compared to bespoke hardware-enabled solutions and potentially introducing resource competition between sensing and communications hardware.

New hardware architectures have allowed for millimeter-scale (mm-scale) motion detection leveraging noncooperative illuminators using architectures like those of traditional active radars. Injection-locked techniques have been shown to be able to extract target motion information using the injection-locking and injection-pulling effects in microwave oscillators [35], [36], [37], [38]. The results of these studies showed that human gestures [35], [37] and vital signs [36], [38] could be detected with custom systems. Other works have shown the ability to detect target motion without using an injection-locked oscillator, instead leveraging a custom mixer to achieve downconversion [39], [40], [41]. The systems were shown to be able to detect mm-scale motions [39], [41], human vital signs [40], and gestures [40] using signals in the 2.4- [39], [40] and 5-GHz [41] Wi-Fi bands. In addition, a beamforming study using this architecture was conducted using two collocated 5-GHz passive radars [42]. However, the study in [42] did not leverage a high number of receiver channels to achieve a practically small angular resolution. Furthermore, the study did not use human targets to detect metrics such as respiration rate, instead adopting an ideal test setup. Finally, nonideal effects were not considered, which can impact the performance of a passive sensor since no signals originate onboard. In this article, a 16-channel beamforming passive radar sensor is presented that operates in the 5-GHz Wi-Fi band to detect small motions with a high degree of angular resolution. The proposed sensor integrates all RF and baseband hardware onboard and leverages a USB link for data processing to determine target angle and motion frequency. This is illustrated in Fig. 1 where the target angle is shown in Fig. 1(a) and the corresponding motion frequency in Fig. 1(b). In addition, the impacts of stationary clutter are analyzed to evaluate the impacts of clutter on passive radar motion sensing.

The rest of this article is organized as follows. Section II provides the theory of beamforming passive radar and analyzes the impacts of nonidealities on motion sensing and beamforming. A simulation study is performed to visualize the impacts of target location, transmitter location, and nonideal effects. Section III discusses the design procedure used to develop the custom beamforming passive radar. Section IV presents the experimental results in a controlled setting and a realistic respiration detection scenario. Conclusions are then drawn in Section V.

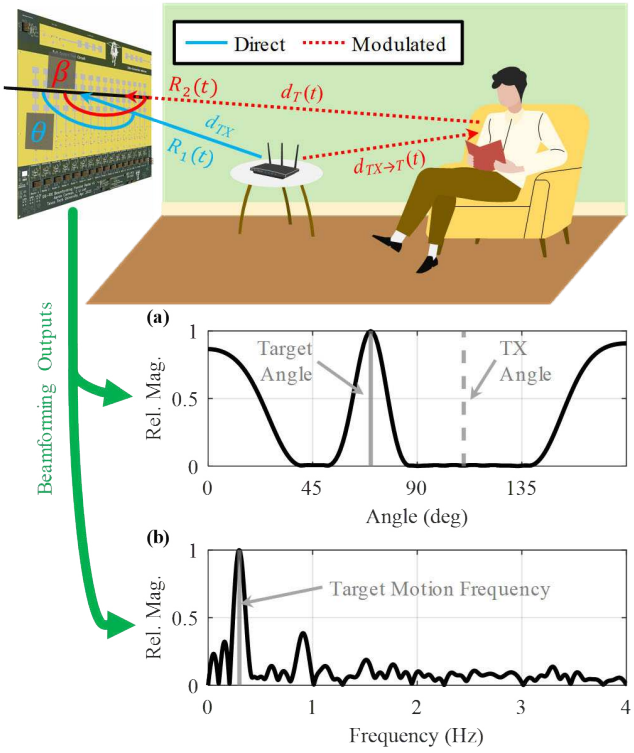

Fig. 1. Example passive sensor used to detect (a) target angle and (b) motion frequency simultaneously. The 16-channel linear array of antennas allows for the detection of target direction while Doppler processing shows motion frequency in the target's direction.

II. Passive Radar Theory

In contrast to traditional active radar techniques, passive sensing relies on ambient EM energy to extract the physical characteristics of targets, removing the need for a dedicated illumination signal. As a result, however, the signal models used in monostatic active radar setups must be modified to account for new effects introduced by the bistatic geometry. This is shown in Fig. 1, where a Wi-Fi access point generates EM energy that creates two paths for received energy: a direct path between the transmitter and radar shown by d_{TX}, and an indirect path where energy is radiated to the target shown by $d_{\mathrm{TX}\to\mathrm{T}}$ then scattered in the direction of the radar shown by d_{T}. The direct path can act as a constant reference since its distance is not modulated, while the indirect path encodes the target's physiological movements, which is used to extract motion frequency.

A. Beamforming and Signal Models

Conventional beamforming techniques rely heavily on analog phase shifters in the transmit and receive signal paths, digital weighting of independent receiver channels, or a hybrid implementation of the two techniques to effectively isolate responses in a cluttered environment and estimate the angle of arrival for a reflected signal. In analog beamforming, a necessary requirement for the phased array is that the phase

shifts should only be applied to the onboard reference to generate a relative phase shift between signals. In passive radar systems with no onboard oscillator, however, it is not feasible to apply a phase shift to only one of the two received signals as both originate off-board and occupy the same bandwidth. As such, analog beamforming cannot be reasonably performed in the proposed system as it is not possible to create a relative phase shift between the direct and modulated signal paths.

Digital beamforming removes the need for analog phase shifters by performing all relative phase shifts in the digital domain. The baseband output of an interferometry system is well-known and by the simple synthesis of an appropriate weighting vector, it is possible to perform beamforming in an entirely digital fashion [43]. Many techniques published in the literature, however, leverage onboard local oscillators (LOs) to provide a known reference signal that is independent of the receive channel (i.e., the LO signal is assumed to be equal in amplitude and phase at every receive channel). Passive sensing, on the other hand, does not use an oscillator and relies exclusively on the path length difference between the unmodulated and phase-modulated signals to produce a baseband response. As a result, the signal models for passive sensing are more complex. For a single passive sensing receiver, the normalized transmit and two received signals from an illuminator of opportunity and target can be represented as

$$T(t) = \cos(2\pi f_c t) \tag{1}$$

$$R_1(t) \propto \cos(2\pi f_c t - k d_{\mathrm{TX}}) \tag{2}$$

$$R_2(t) \propto \cos(2\pi f_c t - k[d_{\mathrm{TX}\to\mathrm{T}}(t) + d_{\mathrm{T}}(t)]) \tag{3}$$

respectively, where $k = 2\pi/\lambda$ is the propagation phase constant, d_{TX} is the distance from the transmitter to the radar, and $d_{\mathrm{TX}\to\mathrm{T}} + d_{\mathrm{T}}$ is the sum of distances between the transmitter and target and the target and radar [44]. Note that the received signals in (2) and (3) are shown in their normalized form to focus on the beamforming aspect of this work. In reality, R_1 and R_2 can differ significantly in amplitude and have large impacts on the design of the receiver, as shown in [40] and [41]. Fig. 1 provides an illustration of the distances in (1)–(3) in the context of a motion-sensing application. In the proposed passive sensing system, the received signals drive a nonlinear element such as a diode to accomplish frequency mixing. After Taylor series expansion of the nonlinear response and low-pass filtering, the baseband response can be written using the following equation:

$$x_{\mathrm{BB}}(t) \propto \cos(k[d_{\mathrm{TX}\to\mathrm{T}}(t) + d_{\mathrm{T}}(t) - d_{\mathrm{TX}}]). \tag{4}$$

If, however, multiple receive antennas are considered as part of a digital beamforming system, this baseband response is modified to account for the slight path differences between adjacent channels. Using the theory from [42] and assuming a sensor with N receive elements numbered from 0 to $N-1$, the two received signals and corresponding baseband response

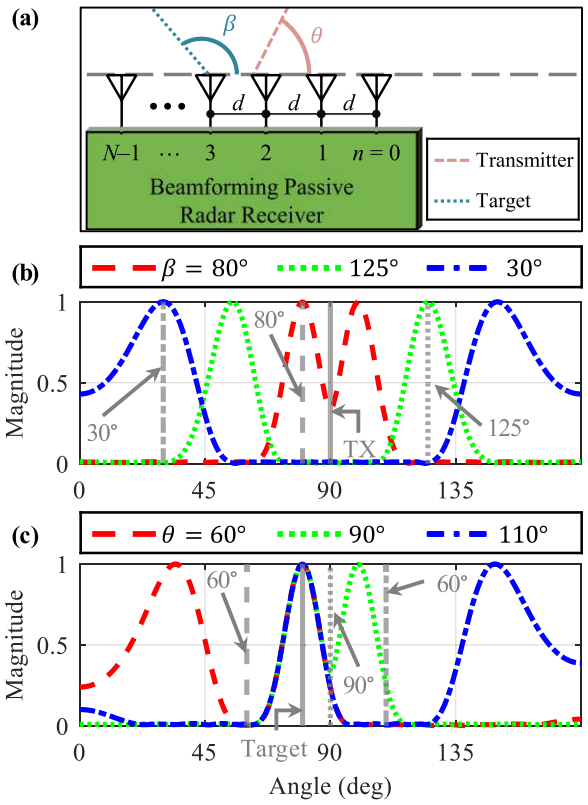

Fig. 2. (a) Passive radar beamforming setup. (b) Dependence on target position can be seen, where a changing target position creates a varying response. (c) Dependence on transmitter position can be seen, where a changing TX location changes the position of the "ghost" target.

at the nth element may be represented as

$$R_1(t) = \cos(2\pi f_c t - k[d_{\mathrm{TX}} + nd\cos(\theta)]) \tag{5}$$

$$R_2(t) = \cos(2\pi f_c t - k[d_{\mathrm{TX}\to\mathrm{T}}(t) + d_{\mathrm{T}}(t) + nd\cos(\beta)]) \tag{6}$$

$$\begin{aligned} x_{\mathrm{BB}}(t) &\propto \cos(k[d_{\mathrm{TX}\to\mathrm{T}} + d_{\mathrm{T}} - d_{\mathrm{TX}} - nd(\cos(\theta) - \cos(\beta)]) \\ &= \cos(k[d_{\mathrm{TX}\to\mathrm{T}} + d_{\mathrm{T}} - d_{\mathrm{TX}}] - n\psi) \end{aligned} \tag{7}$$

where θ and β are the angles to the noncooperative transmitter and target, respectively, d is the distance between antenna elements, and $\psi = kd(\cos(\theta) - \cos(\beta))$ represents the impacts of the phase shifts of both the direct and modulated signals. An illustration of these angles and antenna distances is provided in Figs. 1 and 2(a), where it is seen that the direct and indirect signals both experience a phase shift between elements. When compared to the case of active radar, where it is assumed that an onboard oscillator provides a signal that is equal in phase to all receiver channels (i.e., $\theta = 90°$), (7) reduces to the well-known equation for the relative phase of baseband signals in a receiver array. A weighting vector can then be synthesized to compensate for the effects of ψ and determine the response in a particular direction. This process can be repeated for multiple values of β (and therefore ψ) to visualize the angles that produce a maximum response, thereby providing a visualization of the target's direction.

It is important to note that, if the location of the illuminator of opportunity is unknown, (7) contains two

unknown variables θ and β and will induce a constant error in the angle-of-arrival estimation. As such, it is critical to the operation of the beamforming system to know the relative angle of the transmitter with respect to the radar [42]. In many cases, however, the transmitter position will remain in a fixed location. As a result, this error can be removed through a one-time calibration. Furthermore, since the proposed system cannot employ quadrature demodulation, additional ambiguity is introduced in the baseband signal that ultimately creates a "ghost" target after beamforming. Beginning from (7), the baseband signal can be rewritten using Euler's formula as

$$x_{\mathrm{BB}}(t) = \frac{e^{jkd(t)-jn\psi} - e^{-jkd(t)+jn\psi}}{2} \tag{8}$$

where $d(t)$ represents the time-varying component of the baseband signal created by target motion. If a beamforming weight of $e^{jn\psi}$ is applied, the left component constructively interferes to produce a large response in the beamforming spectrum. If, however, a value of $e^{-jn\psi}$ is applied during beamforming, the right component of (8) constructively interferes to produce a large response, creating the "ghost" target due to the lack of I/Q information. In addition, since the periodic motion $d(t)$ induces positive and negative frequencies after beamforming, it is not possible to distinguish the real target based on the sign of the resulting motion frequency.

To visualize these effects, a simulation study is conducted where the target and transmitter position is varied. For the first study, the target angle β is simulated at 80°, 125°, and 30°, with the transmitter at a fixed position of 90°. The results of these effects are shown in Fig. 2(b) along with the previously known target locations, where the true target position and "ghost" target positions are seen to move in the beamforming output proportional to the true position. A second study is then conducted with a fixed target at 80° and the transmitter angle θ set to 60°, 90°, and 110°. The results of this study are shown in Fig. 2(c), where, to measure the target's true position, the transmitter position must be known in each case. In addition, it is also shown in Fig. 2(c) that the position of the "ghost" target can be modified by changing the location of the transmitter, providing a route for accurate detection by selecting the location of the transmitter and radar such that the "ghost" target angle lies outside the boundaries of the sensing environment.

B. Noise and Clutter Effects

Compared to active monostatic radar systems, where the illumination signal originates onboard, the outputs of passive bistatic radar are inherently lower in magnitude due to several reasons. First, as was described in [41], the radar cross section (RCS) of a target for bistatic passive radar is heavily dependent on the specific arrangement of the sensing environment. If, for example, a target is directly between the transmitter and passive radar receiver, very little of the signal encoding target motion is received by the sensor. Second, since a great majority of energy may be scattered away from the passive radar, large clutter could create strong

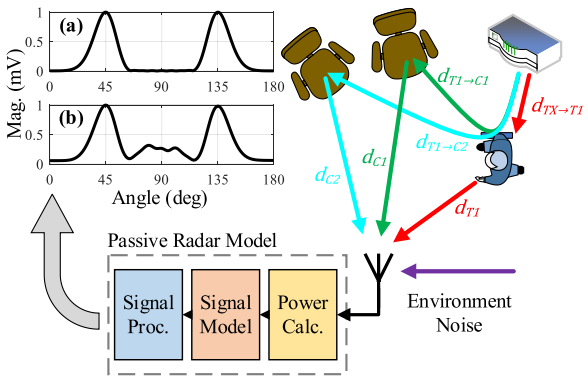

Fig. 3. Passive sensing noise and clutter simulation block diagram. All multipaths containing target motion information are considered, along with environmental and circuit noise. (a) Ideal results are degraded after considering the impacts of (b) noise and clutter.

responses during the angle-of-arrival estimation that obscure the true target due to multipath reflections. Finally, since the reference signal originates offboard and is subject to path loss described by the Friis equation, the magnitude of the reference signal may not be sufficient to drive the downconversion mixer, increasing the conversion loss. As a result of these effects, the inclusion of clutter (and thereby multipath) and noise effects is extremely important when modeling the performance of passive radar beamforming systems.

To evaluate the impacts of nonidealities on passive sensing performance, noise and clutter models are introduced to previously develop passive sensing models, with an overall simulation diagram including key parameters shown in Fig. 3. Noise is modeled as white additive Gaussian noise occupying the frequency bands of interest and added in the RF front end and baseband circuitry with considerations of environmental, thermal, and flicker noise. Stationary clutter creates strong dc outputs due to multipath reflections from the transmitter to the clutter then to the receiver that must be mitigated in dc-coupled systems. In addition, the signal scattered by the target can also experience multipath effects, as illustrated in Fig. 3. If an ac-coupled system is considered, however, the dc response produced by transmitter–clutter–receiver multipath is rejected before being digitized. The transmitter–target–clutter–receiver multipath, on the other hand, includes ac information that will not be filtered before digitization and signal processing, which can impact beamforming if the multipath signal is stronger than the reflected signal. Coupled with the fact that a target may naturally scatter more energy in the direction of a strong clutter, the impacts of strong clutters and multipath can have a large impact on angle estimation, especially if the multipath signal is stronger in magnitude. In a similar case, the presence of multiple transmitters can introduce similar impacts after beamforming. Expressions for received power from targets and clutters are updated in this work to account for the multipath effects in passive sensors. Fig. 3 can be used as a reference to illustrate the distances mentioned in this derivation. In the case of power received from the ith target, the following expression is used to account for the

bistatic geometry:

$$P_{RX} = \frac{P_{TX} G_{TX} G_{RX} \sigma_T(i) \lambda^2}{(4\pi)^3 d_{TX\to T}^2(i) d_T^2(i)} \tag{9}$$

where P_{TX} is the transmit power, G_{TX} and G_{RX} are the transmit and receive antenna gains, respectively, $\sigma_T(i)$ is the RCS of the ith target, λ is the free-space wavelength of the carrier, and $d_{TX\to T}$ and d_T are the ith target's transmitter–target and target–radar distances. In the case of clutter, a second equation is developed as part of this work. In a similar derivation to the radar equation, the power reflected by the ith target in the direction of the jth clutter is represented as

$$P_{T\to C} = S_T \sigma_{T\to C} = \frac{P_{TX} G_{TX} \sigma_{T\to C}(i,j)}{4\pi d_{TX\to T}^2(i)} \tag{10}$$

where $\sigma_{T\to C}$ is the RCS value that characterizes the amount of power reflected toward a given clutter. The value of $\sigma_{T\to C}$ in this equation is not equal to the value of σ_T in (9) since a target may naturally scatter more energy in one direction. Considering the RCS of the clutter, the free-space path loss from the clutter to the sensor, and the sensor's antenna gain, the power received due to the clutter at the sensor is represented as

$$P_C = \frac{S_C \sigma_C(i,j) \lambda^2}{(4\pi)^2 d_C^2} = \frac{P_{TX} G_{TX} \sigma_{T\to C}(i,j) \sigma_C(i,j)}{(4\pi)^4 d_{TX\to T}^2(i) d_{T\to C}^2(i,j) d_C^2(j)} \tag{11}$$

where σ_C is the RCS that relates the amount of power from the ith target reflected by the jth clutter, and $d_{T\to C}$ and d_C are the jth clutter's target–clutter and clutter–radar distances. In the case of multitarget/clutter scenarios, this equation can be expanded to evaluate the impacts of multiple targets with multiple clutters. The angle of arrival may also be considered. The closed-form solution for the received signal at the nth channel is given as

$$v_{RX}(t) \propto \sum_{i=1}^{N_T} \sqrt{P_{RX}(i)} \cos(k \Delta d_T(i) n \psi(i)) + \sum_{i=1}^{N_T} \sum_{j=1}^{N_C} \sqrt{P_C(i,j)} \cos(k \Delta d_C(i,j) n \psi(j)) \tag{12}$$

$$\Delta d_C = d_{TX\to T} + d_{T\to C} + d_C - d_{TX} \tag{13}$$

$$\Delta d_T = d_{TX\to T} + d_T - d_{TX} \tag{14}$$

where Δd_C is the path length difference between the transmitter–target–clutter–radar path and the direct path shown in (13), Δd_T is the path length difference between the direct and transmitter–target–radar paths in (14), d_{TX} is the distance from the transmitter to the radar, and ψ is the phase shift between antenna elements. Note that both Δd_C and Δd_T encode target motion, highlighting the impact of static clutters if P_C is close to or greater than the magnitude of P_{RX}.

The impacts of stationary clutter on sensing a target moving with a 2-cm amplitude at 45° can be observed in Fig. 3. In the ideal case shown in Fig. 3(a), only the target and "ghost" target produced by the lack of I/Q data can be seen. In the nonideal result in Fig. 3(b), which includes a large clutter at 90° and 20 evenly distributed clutters in the surrounding environment such as walls, furniture, and appliances, the ideal results in Fig. 3(a) are modified considerably. Primarily, the impacts of the large clutter at 90° creates an elevated noise level in that direction, while the distributed clutters raise the baseline noise levels outside the direction of the target.

It is worth noting that, in addition to the effects of clutter and noise detailed above, the presence of additional nonidealities such as multiple transmitters or varying data modulation techniques can have further impacts on the final beamforming results. As a result, the specific nature of a sensing environment should be evaluated to determine if the presence of multiple transmitters or severe multipath effects could have a negative impact on passive radar beamforming.

III. Beamforming Passive Sensor Design

A. Substrate Model

To verify the proposed theory in a rigorous fashion, a 16-element 1-D beamforming passive sensor is developed based on the architecture first proposed in [39] to operate in the 5.8-GHz industrial, scientific, and medical (ISM) band. The system is developed on ISOLA FR4 substrate, which reports a dielectric constant of 4.3 and a loss tangent of 0.019. These metrics, however, are not measured in the band of interest and lead to inaccuracies in development. Ultimately, a dielectric constant of 4.8 was used during development as this provided better agreement between simulated and experimental results.

B. Array Design

To perform effective beamforming and angle-of-arrival estimation without introducing grating lobes, adjacent antenna elements in the linear receive array should be placed a maximum of $\lambda/2$ m from each other. This is not a requirement as many works have demonstrated effective beamforming using nonuniform arrays where adjacent antenna elements can be separated with distances greater than $\lambda/2$ [25], [45], [46]. For this work, however, the passive radar receiver array will be designed with all antennas uniformly spaced with a pitch less than $\lambda/2$. As was mentioned in Section III-A, the beamforming passive radar is designed to operate in the 5.8-GHz ISM band with an associated free-space wavelength of 51.72 mm. As such, the passive radar receiver array is designed with an element pitch of 25 mm to provide a margin of error to support manufacturing tolerances.

To provide the maximum beamforming angular resolution while simultaneously ensuring a practical sensor size for experimentation, the beamforming passive radar developed in this work is designed with 16 independent receiver channels. Furthermore, to simplify the physical layout of the beamforming passive radar, all receiver components including the antenna, RF front end, and baseband amplifiers will be designed with a physical width of less than 25 mm. If this criterion is met, the physical layout can be accomplished by simply tiling each unit receiver with the appropriate spacing, without introducing the potential for inadvertent short circuits. Supporting electronics that are not repeated for

every unit receiver such as power conditioning and analog-to-digital converters (ADCs) are individually routed. In addition, several test structures are included onboard to allow testing of individual receiver elements without the effects of mutual coupling between adjacent array elements.

C. Antenna Design

To measure the ambient EM energy, an onboard antenna element is developed and used for each element in the receiver array. The design of the antenna is nontrivial since many competing metrics introduce tradeoffs that must be considered during design. Primarily, the relationship between the antenna aperture and pitch must be considered, as an increase in the antenna aperture of an array element can improve the receiver sensitivity while also increasing the pitch between receiver elements. Furthermore, since the passive sensor is developed to accomplish 1-D beamforming, a wider beamwidth for array elements is desired in the beamforming plane to maximize the field-of-view (FOV) of the sensor. As a result, to preserve the half-wavelength spacing between elements and support a large FOV, a series patch antenna is used to increase the antenna aperture by adding more elements vertically, while maintaining a sufficiently small horizontal width that supports a half-wavelength pitch between elements. The series patch antenna is designed using Applied Wave Research (AWR) Axiem to find dimensions that produce sufficiently low reflection at the desired operating frequency. Following this step, the antenna dimensions are then optimized to provide a good input match and an acceptable radiation pattern for 1-D beamforming. The simulated and measured antenna characteristics after this optimization are shown in Fig. 4. From the graph in Fig. 4(a), the reflection coefficient at the 5.8-GHz center frequency is seen to be sufficiently low for experimental testing while the radiation pattern in Fig. 4(b) highlights the wide beamwidth in the H-plane and the narrower beamwidth in the E-plane due to the series patch elements.

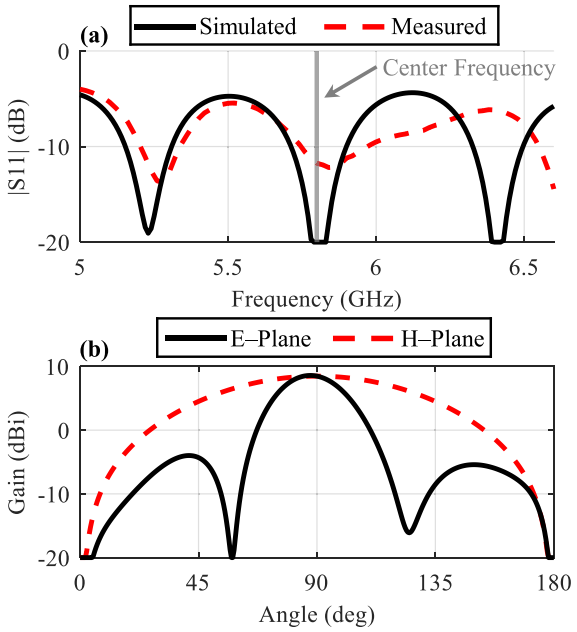

Fig. 4. Series patch antenna results. (a) Simulated and experimental S_{11} show a good match at the design frequency. (b) Radiation pattern shows the omnidirectional pattern in the H-plane and narrower beamwidth in the E-plane.

D. RF Front End

The RF signals detected by the antenna array are quite small in magnitude, and as such require amplification to drive the mixer into its nonlinear operating region. To highlight this, a bistatic case is considered with the transmitter, target, and radar at each vertex of an equilateral triangle with 2-m side length and a transmit power of 15 dBm, antenna gains of 8 dBi, and a target RCS of 0.1 m^2. Using (9) and the free-space path loss formula, the signal received directly from the transmitter is -22 dBm, while the signal encoding target motion is only -49 dBm. As a result, amplification is needed to ensure sufficient downconversion. To address this need, a discrete LNA is developed using the BFP740ESD transistor. The LNA is designed using AWR design environment to perform the input and output matching as well as find an optimal tradeoff between noise figure and gain. Intuitively, a low noise figure may be necessary if the received signals are sufficiently weak compared to environmental and electronic noise. Reducing the noise figure, however, can have the effect of reducing the transducer gain of the amplifier, which can create problems in the passive architecture when the signals are relatively weak in power. Primarily, since no RF signals originate onboard, the received signals must be sufficiently amplified to produce nonlinearity at the mixer. As a result, during the design of the RF front end, the transducer gain is prioritized over the noise figure of the LNA. Furthermore, the proximity of the transistor's pins combined with the thick substrate introduces coupling effects that must be accounted for. As a result, the system is first simulated using closed-form models for planar transmission lines, then extracted using AWR Axiem to account for coupling. After extraction, the stability of the amplifier decreased, requiring a gain reduction to prevent oscillation.

In addition to the LNA, a one-port mixer is developed to convert the two received signals into a single baseband output that can be used to detect motion and perform beamforming. Since the mixer does not require an LO and RF port, the design of the mixer is comparatively simple. The BAT2402-LS diode from Infineon, Neubiberg, Germany, is used to provide the nonlinearity needed for downconversion, along with passive components and transmission line structures to provide an improved match to the LNA output. Like the design of the LNA, closed-form models for input and output matching networks are first leveraged to obtain a first-order solution. EM extraction is then performed to account for second-order effects. During this process, the BAT2402-LS operating point is also swept to find a biasing point that provides an acceptable combination of low conversion loss at the power levels of interest and a good impedance match to the output of the LNA. It is worth noting that, since the RF front end is a custom design for this work, the LNA output port and mixer input port do not necessarily need to be matched to 50 Ω. As a result, the

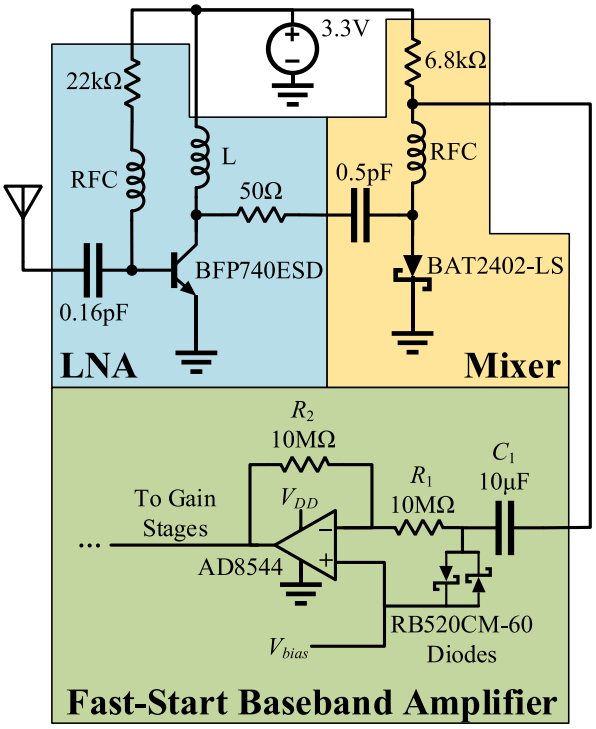

Fig. 5. RF front-end schematic and fast-start amplifier circuit in each of the 16 receiving channels. The LNA amplifies the RF signals to drive the custom mixer to downconvert the received signals to the baseband. The fast-start circuit allows rapid charging of C_1, shortening the startup time of the amplifier.

output impedance of the LNA and the input impedance of the mixer can be modified to allow for improved power efficiency and performance in the RF front end. Furthermore, since none of the signals used in downconversion originate onboard and both occupy the same narrow bandwidth, I/Q demodulation is not possible with existing architectures. As a result, the output signal from the mixer, represented in (7), contains only the in-phase component of the RF signal. This ultimately introduces ambiguities due to the symmetry of the cosine function and prevents perfect reconstruction of the target motion. The final RF front-end design is shown in Fig. 5, with the LNA and single-diode mixer sections highlighted with accompanying passive components.

To characterize the ability of the RF front end to amplify the received signals and downconvert to the baseband, a two-tone test setup is used. An RF front-end test board consisting of the LNA and the single-diode mixer is fed with two 5.8-GHz signal generators that are offset in frequency. This frequency offset creates a constant IF output frequency after downconversion, allowing for rapid measurement of the output voltage amplitude. To improve the accuracy of the measurements, a simple baseband amplifier with a known gain is used to amplify the mixer output signal. The voltage of both tones at the RF front-end test board input port is swept, and the output peak-to-peak voltage is recorded after amplification. The results are then decoupled from the baseband amplifier's gain to characterize the RF front-end's ability to amplify and downconvert signals. The 2-D interpolation is then used to create Fig. 6. From the results, the output voltage shows a

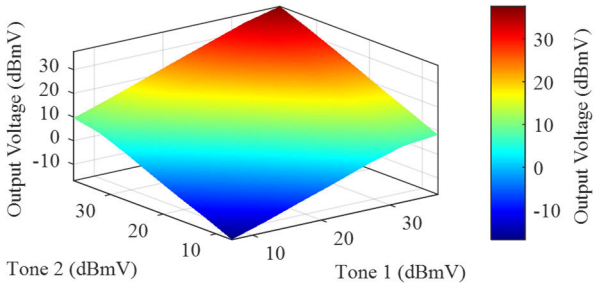

Fig. 6. RF front-end two-tone downconversion results. Like traditional mixer design, a higher input voltage at the RF front-end input port creates more nonlinearity and improves the conversion gain of the RF front end.

dependence on both input tone signal strengths, highlighting the importance of RF gain to drive the mixer for sufficient downconversion. If, for example, a lower received signal power is expected, more RF gain can be added to the system to ensure that enough conversion gain is provided at the mixer.

E. Baseband Amplifier and Digitization

After downconversion to the baseband, the radar output signal is on the order of mV. Direct sampling is feasible with modern ADCs but requires careful design to ensure low noise levels and effective sampling. Instead of relying on precision ADCs, a more effective solution would be to leverage baseband amplifier architectures to increase the amplitude of the radar's output signal to acceptable levels. AC-coupled designs are typically leveraged since the radar's dc output could be orders of magnitude larger than the signal of interest. Baseband amplifier design for low-frequency signals such as those produced by human activities comes with inherent tradeoffs, however, primarily between lower cutoff frequency and startup time. This is a result of the inverse relationship between the formulas for lower cutoff frequency and time constant, which are given in (15) and (16), respectively, where R_1 and C_1 are the values of the input capacitor and resistor, respectively, as shown in Fig. 5. From the equations, it can be seen that a short-time constant correlates to a high cutoff frequency, which is detrimental when the frequencies of interest are less than 1 Hz

$$f_C = \frac{1}{R_1 C_1} = \frac{1}{\tau} \tag{15}$$

$$\tau = R_1 C_1. \tag{16}$$

Many previous works have leveraged modern software capabilities [47] or dc-coupled adaptive amplifier architectures [3], [48] to remove the dc component of the received signal while amplifying the ac signals of interest. These techniques, however, require many new hardware components to be added or require more advanced signal processing. Instead of leveraging these techniques, the fast-start baseband amplifier architecture in [49] is used due to its simplicity and low cost compared to other designs. The architecture is shown in Fig. 5, where the included fast-start diodes provide a path for rapid charging upon startup. Using the architecture, the startup

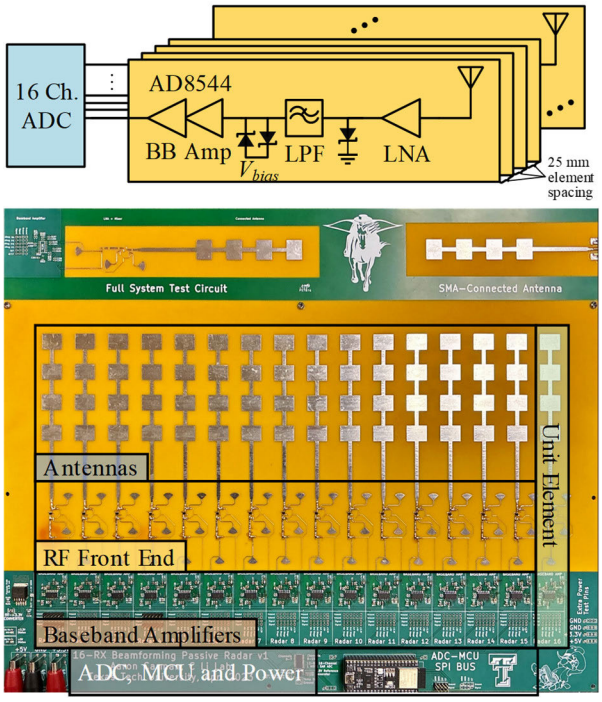

Fig. 7. Final beamforming passive radar block diagram and fabricated device. The 1-D structure of the unit element allows for tiling to be used to simplify the layout, so long as the unit element width is less than 25 mm.

time of the radar's baseband amplifiers can be shortened considerably. On the other hand, since accurate displacement reconstruction is not possible with the proposed architecture due to the lack of I/Q data, dc components created by target motion are not required to be preserved, making the employed fast-start architecture an ideal solution for this radar. A pair of RB520CM-60 Schottky diodes are used to provide the desired fast start, and the proceeding amplifier stages are configured to provide 40-dB total baseband gain. The final stage of each baseband amplifier configured as a unity gain buffer to provide a low output impedance to the ADC.

After baseband amplification, the amplified signals are digitized using the ADS7953 ADC from Texas Instruments, Dallas, TX, USA. The ADS7953 was selected due to its high maximum sampling rate of 1 MS/s, 12-bit precision, and 16 input channels, which allows for the radar output signals to be digitized with sufficient precision and speed for future batch processing without needing multiple ADC chips in parallel. It is important to note during design that the ADC maximum sampling frequency is shared among all channels. As such, if each channel is sampled equally, the maximum per channel sampling rate is 62.5 kS/s. The ADC is programed via a serial peripheral interface to automatically step through each of the 16 radar outputs. The ADC output is then stored by an Espressif Systems ESP32-S2 microcontroller development board and sent to a computer through a universal asynchronous receiver-transmitter (UART) interface. The output data are then recorded by the computer for bulk processing. The final radar block diagram can be seen in Fig. 7, with key components highlighted to show how the radar elements can be tiled if the unit widths are sufficiently small.

IV. Experimental System Results

To evaluate the system-level performance of the developed beamforming passive sensor, two experiment strategies are employed. First, to provide a controlled test that is decoupled from the scattering characteristics of a real target, two cooperative continuous wave (CW) microwave sources are used to induce a known and well-controlled response in the baseband signal. This controlled experiment will ultimately allow for an initial assessment of the beamforming model's performance with a higher number of channels compared to previous works, while also minimizing the impacts of noise, clutter, and target characteristics which may be cumbersome to measure otherwise. Following this first experiment, a second series of experiments is used to determine the passive radar's performance in a respiration rate measurement scenario, where a real human target's respiration rate can be measured along with the target's angle relative to the radar sensor. Before experimental testing, the radar is characterized in situ to establish operating parameters. The antenna realized gain is found to be approximately 4 dBi, with a half-power beamwidth of 74° in the H-plane and 30° in the E-plane. The RF front-end gain is found to range from -20 to $+2$ dB in the operating region of interest, depending on the input signal strengths. The simulated noise figure of the LNA and mixer are found to be 2.6 and 15 dB, respectively.

A. Experiment With Cooperative Sources

For the initial experiment, two cooperative microwave sources along with accompanying antennas are leveraged to create a known baseband response. One source emulates the direct signal from a noncooperative transmitter to the passive radar receiver and will be called the "direct source." The other transmitter is synchronized to the direct source and is offset in frequency to produce a known baseband response like that of a moving target. This transmitter can then be placed at different locations to assess the angle-of-arrival estimation performance. As such, the second transmitter will be called the "target source." Both sources transmit signals in the 5.8-GHz ISM band at a power level of 10 dBm. The frequency offset for this experiment is 2 Hz. When enabling both the direct source and target source, the passive sensor will receive two signals that, after downconversion, produce a sinusoidal baseband response with a frequency equivalent to the frequency difference between the two sources. As the target source is physically moved in the sensing environment, the response after beamforming is expected to change due to the relative phase difference between adjacent elements. At each step, the passive radar collects and stores the corresponding baseband data for bulk processing. The data are then compared against simulation results to verify the accuracy of the proposed models in a high angular resolution system and reveal nonidealities present in the sensor.

To reduce the impacts of human measurement error, a grid layout is used for this experiment, illustrated in Fig. 8 by a top–down illustration and an image of the experimental setup. In this layout, the passive sensor is the origin, while

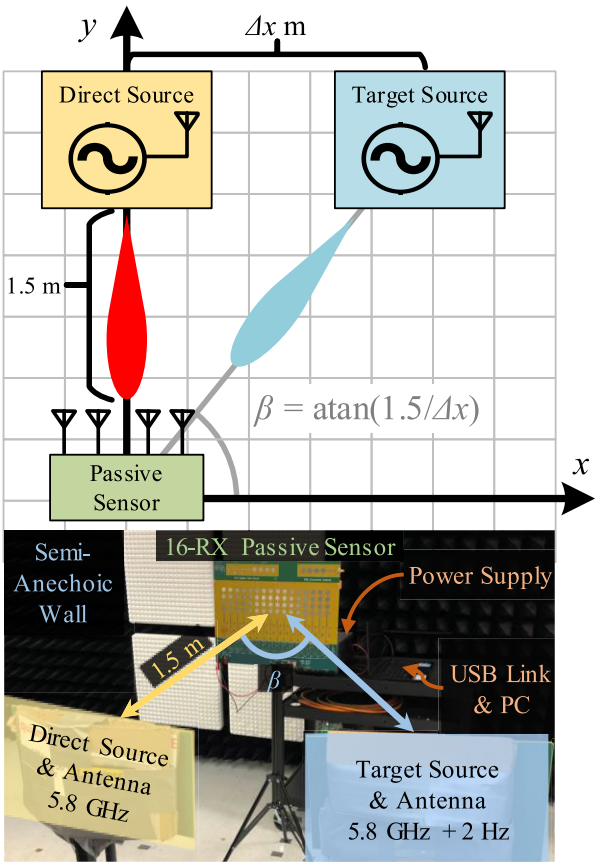

Fig. 8. Controlled experimental setup. The grid layout allows for precise angle measurements using trigonometric functions, reducing the impacts of human error on ground-truth angle measurement.

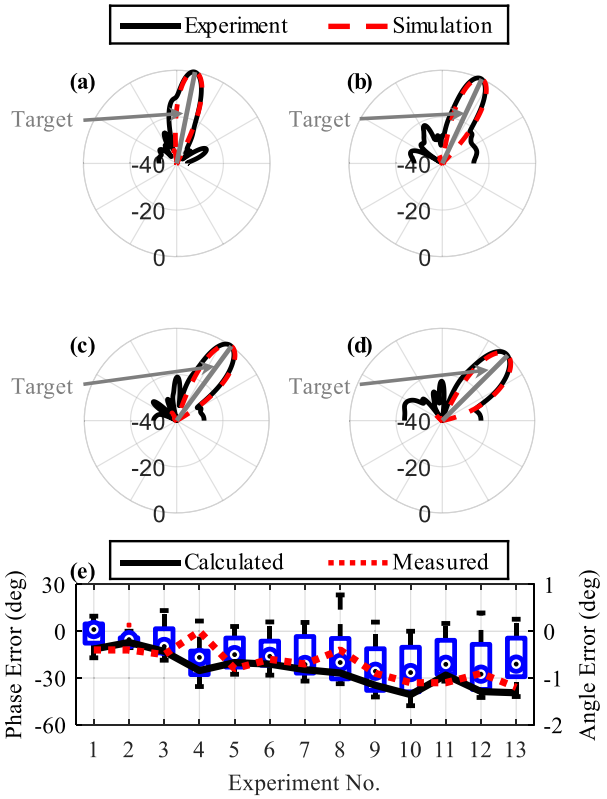

Fig. 9. Cooperative microwave source experimental results. (a)–(d) Results show good agreement with simulated results for a target in the same position, while (e) phase errors that result in a low angle-of-arrival error compared to ideal values.

the direct and target sources maintain a constant y-coordinate of 1.5 m. The direct source is held at the 90° direction for this case, and as such remains fixed at the (0 m, 1.5 m) coordinate. Due to the sizes of the transmitting antennas, the target source is first placed at a coordinate of (0.3 m, 1.5 m), and its x-value is increased by 0.1 m for each experiment until reaching 1.5 m. This corresponds to an angle-of-arrival sweep from 79° to 45°, with a total of 13 steps. A sample of angle-of-arrival measurements is given in Fig. 9(a)–(d), where it is seen that the measured results show a high degree of agreement with the simulation results. In all cases, the noise levels outside of the main lobe are at least 20 dB smaller in magnitude compared to the response induced by the target source. In addition, the phase error of the received signals is shown in Fig. 9(e) as a box and whisker plot. Although the recorded phase error reaches a maximum of 51°, it can be shown that this corresponds to a relatively low angle error and can be explained by human error and the relatively low precision with which ground-truth angles can be measured in the experimental environment. To provide a more useful and intuitive measure of the sensor's accuracy, the maximum phase error can be converted to a corresponding target angle error. The phase error can be written as

$$\Delta\phi = (N-1)kd\big(\cos(\theta') - \cos(\theta)\big) \tag{17}$$

where θ is the measured target angle and θ' is the target's true angle. In (17), all values except θ' are known or measurable. After algebraic manipulation, the angle error can be expressed as

$$\Delta\theta = \theta' - \theta = \operatorname{acos}\left(\frac{\Delta\phi}{nkd} + \cos(\theta)\right) - \theta. \tag{18}$$

The angle error can also be found directly by comparing the largest peak after beamforming to the target's measured angle, allowing for a comparison between the calculated values in (18) with the experimental results. Both the measured and calculated angle errors can be found in Fig. 9(e), where it is seen that despite the larger phase deviations present between receivers, the corresponding angle errors are quite low.

It is worth noting that, compared to previous works, the results in Fig. 9 show no clear ambiguity or "ghost" targets compared to the results in Fig. 2 or 3. This is a byproduct of the use of cooperative sources, and the fact that the output in such an experiment is a perfect continuous sinusoid with a periodic phase delay between elements. Beginning from (8), the received baseband signal equations can be modified to account for the frequency difference between the two tones. The new baseband signal equation is then

$$x_{\mathrm{BB}}(t) = \frac{e^{j\Delta ft - jn\psi} - e^{-j\Delta ft + jn\psi}}{2} \tag{19}$$

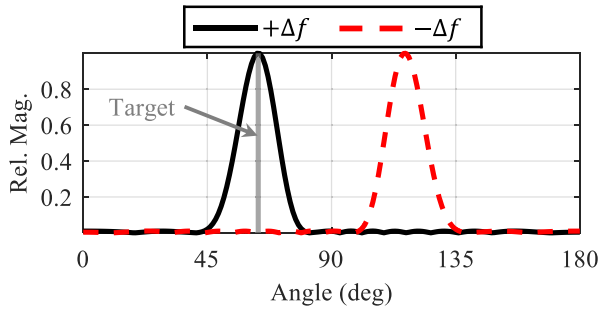

Fig. 10. Impact of Δf on beamforming results. Although there appears to be no ambiguity, changing the sign of Δf can change the beamforming results without physically moving the target.

where Δf is the frequency difference of the two microwave tones. After applying the beamforming weights $e^{jn\psi}$, only the positive frequency component remains. If, however, the beamforming weights $e^{-jn\psi}$ are applied, only the negative frequency component remains. Coupled with the fact that the beamforming algorithm measures only positive frequencies when determining target location, the use of cooperative sources removes the previously seen ambiguities. Accurate angle measurement, however, relies upon knowing whether the frequency difference between two sources is positive or negative. If, for example, the Δf is changed from $+2$ to -2 Hz, the measured angle would be mirrored around 90° since the beamforming algorithm measures positive frequencies. This is shown in Fig. 10, whereby simply changing the sign of Δf, the beamforming results give incorrect measurements for the target at 60° using cooperative sources.

B. Experiment of Respiration Detection

To evaluate the sensor's performance in a practical application, the sensor is used to detect a breathing target's direction relative to the radar sensor in a realistic environment. In this case, a human test subject is seated approximately 1 m to the passive radar sensor, with the radar aligned to the subject's approximate chest level. A CW microwave source produces ambient EM energy at a frequency of 5.8 GHz at a power of 10 dBm, also aligned to the same height as the passive sensor and the subject's chest. It is worth noting that the transmitter in this case does occupy spectrum resources. In a practical case, however, an "always-on" signal such as the pilot carrier in 802.11 Wi-Fi could be used to provide illumination. The subject is seated at approximately 150°. Data are collected for approximately 12 s. The experimental setup for respiration detection is shown in Fig. 11.

The subject is first instructed to breathe at a normal rate, to assess the passive radar's performance in both angle-of-arrival estimation and motion frequency measurement. The results of this study are shown in Fig. 12. From the beamforming results in Fig. 12(a), it is seen that the passive sensor isolated the direction of the moving target. This is confirmed by calculating the fast Fourier transform (FFT) of the signal toward the peak of the beamforming results, as shown in Fig. 12(b), where the target's respiration frequency

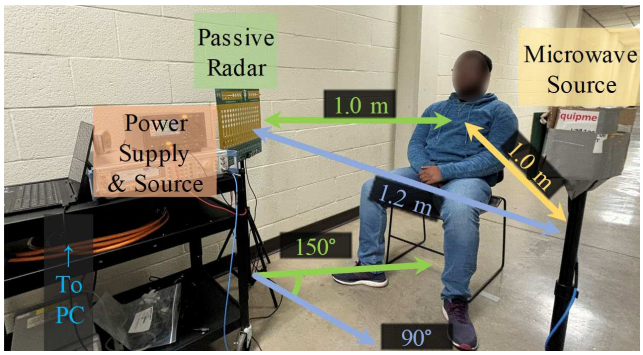

Fig. 11. Respiration detection experimental setup. A microwave source generates ambient energy that is reflected by the target at 150° and received by the radar. The radar then measures target angle and motion frequency.

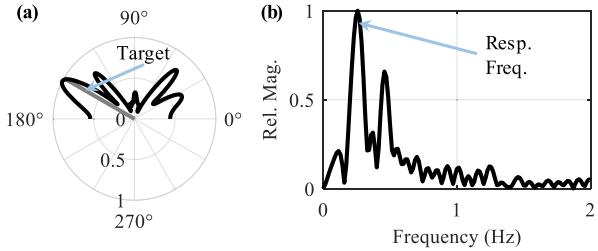

Fig. 12. Experimental results with subject breathing normally. (a) Target direction can be seen after beamforming. (b) Subject's respiration frequency can be found by calculating the FFT in the target's direction.

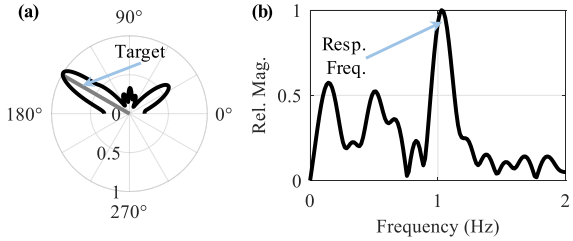

Fig. 13. Experimental results with subject breathing at an elevated rate. (a) Once again, the target direction can be seen. (b) Subject's higher respiration rate can also be found.

of approximately 0.25 Hz can be seen. It can also be seen that the ambiguity discussed in Section III-D is present but is not perfectly symmetric about the 90° point. This is due to the target's unintentional motion toward or away from the sensor during the experiment, which creates an uneven response like that discussed in Section IV-A.

A second experiment is also conducted in a similar manner, but with the target now instructed to breathe at an elevated rate. As a result, it is expected that the beamforming output of this experiment will be like the previous case, but with an increase in motion frequency measured at the peak angle. The results of this experiment are shown in Fig. 13. From the beamforming results in Fig. 13(a), a much clearer target can be seen because of the increased respiration rate. This is likely due to the increased chest wall motion that occurs when breathing is elevated. In addition, the frequency-domain results in Fig. 13(b) show that the increased respiration rate of approximately 1 Hz can be extracted, demonstrating the

sensor's ability to concurrently determine a target's angle of arrival and motion frequency.

V. Conclusion

This article presented a 16-channel beamforming passive radar that can be used in an indoor environment to detect a moving target's angle and motion. The sensor leverages a single noncooperative transmitter in the 5-GHz Wi-Fi band and a digital beamforming approach to measure target characteristics. The theory of passive radar beamforming was presented and verified through an experimental setup, where a target's respiration frequency and angle were measured. The experimental results demonstrate the passive radar's ability to detect target motion using third-party illuminators of opportunity for a scalable approach to indoor sensing.

References

[1] C. Li et al., "A review on recent progress of portable short-range noncontact microwave radar systems," *IEEE Trans. Microw. Theory Techn.*, vol. 65, no. 5, pp. 1692–1706, May 2017.

[2] C. Li, V. M. Lubecke, O. Boric-Lubecke, and J. Lin, "A review on recent advances in Doppler radar sensors for noncontact healthcare monitoring," *IEEE Trans. Microw. Theory Techn.*, vol. 61, no. 5, pp. 2046–2060, May 2013.

[3] D. Tang, J. Wang, W. Hu, Z. Peng, Y. Chiang, and C. Li, "A DC-coupled high dynamic range biomedical radar sensor with fast-settling analog DC offset cancelation," *IEEE Trans. Instrum. Meas.*, vol. 68, no. 5, pp. 1441–1450, May 2019.

[4] Z. Peng and C. Li, "Portable microwave radar systems for short-range localization and life tracking: A review," *Sensors*, vol. 19, no. 5, p. 1136, Mar. 2019.

[5] C. Gu, J. Wang, and J. Lien, "Motion sensing using radar: Gesture interaction and beyond," *IEEE Microw. Mag.*, vol. 20, no. 8, pp. 44–57, Aug. 2019.

[6] J. Hasch, E. Topak, R. Schnabel, T. Zwick, R. Weigel, and C. Waldschmidt, "Millimeter-wave technology for automotive radar sensors in the 77 GHz frequency band," *IEEE Trans. Microw. Theory Techn.*, vol. 60, no. 3, pp. 845–860, Mar. 2012.

[7] R. Amar, M. Alaee-Kerahroodi, and P. Babu, "Optimized-slope FMCW waveform for automotive radars," in *Proc. 23rd Int. Radar Symp.*, Gdansk, Poland, 2022, pp. 110–115.

[8] T. T. Braun, J. Schöpfel, P. Kwiatkowski, C. Schweer, K. Aufinger, and N. Pohl, "Expanding the capabilities of automotive radar for bicycle detection with harmonic RFID tags at 79/158 GHz," *IEEE Trans. Microw. Theory Techn.*, vol. 71, no. 1, pp. 320–329, Jan. 2023.

[9] S. Guan, J. A. Bridge, C. Li, and N. J. DeMello, "Smart radar sensor network for bridge displacement monitoring," *J. Bridge Eng.*, vol. 24, no. 1, Jan. 2019, Art. no. 04018102.

[10] D. V. Q. Rodrigues, D. Zuo, and C. Li, "Wind-induced displacement analysis for a traffic light structure based on a low-cost Doppler radar array," *IEEE Trans. Instrum. Meas.*, vol. 70, pp. 1–9, 2021.

[11] O. B. Akan and M. Arik, "Internet of radars: Sensing versus sending with joint radar-communications," *IEEE Commun. Mag.*, vol. 58, no. 9, pp. 13–19, Sep. 2020.

[12] P. Nallabolu and C. Li, "A frequency-domain spoofing attack on FMCW radars and its mitigation technique based on a hybrid-chirp waveform," *IEEE Trans. Microw. Theory Techn.*, vol. 69, no. 11, pp. 5086–5098, Nov. 2021.

[13] H. Kuschel, D. Cristallini, and K. E. Olsen, "Tutorial: Passive radar tutorial," *IEEE Aerosp. Electron. Syst. Mag.*, vol. 34, no. 2, pp. 2–19, Feb. 2019.

[14] M. Weiß, "Compressive sensing for passive surveillance radar using DAB signals," in *Proc. Int. Radar Conf.*, Oct. 2014, pp. 1–6.

[15] D. Gromek, P. Samczynski, K. Kulpa, P. Krysik, and M. Malanowski, "Initial results of passive SAR imaging using a DVB-T based airborne radar receiver," in *Proc. 11th Eur. Radar Conf.*, Oct. 2014, pp. 137–140.

[16] M. Ummenhofer, J. Schell, J. Heckenbach, H. Kuschel, and D. W. D'O Hagan, "Doppler estimation for DVB-T based passive radar systems on moving maritime platforms," in *Proc. IEEE Radar Conf. (RadarCon)*, May 2015, pp. 1687–1691.

[17] B. Tan and B. Sun, "Using Wi-Fi signal as sensing medium: Passive radar, channel state information and followups," 2022, *arXiv:2201.03005*.

[18] B. Tan, Q. Chen, K. Chetty, K. Woodbridge, W. Li, and R. Piechocki, "Exploiting WiFi channel state information for residential healthcare informatics," *IEEE Commun. Mag.*, vol. 56, no. 5, pp. 130–137, May 2018.

[19] X. Li, Z. Deng, F. Yang, X. Zheng, L. Zhang, and Z. Zhou, "WiFi indoor location method based on RSSI," in *Proc. 11th IEEE Int. Conf. Intell. Data Acquisition Adv. Comput. Syst., Technol. Appl. (IDAACS)*, vol. 2, Cracow, Poland, Sep. 2021, pp. 1036–1040.

[20] S. Sigg, S. Shi, F. Buesching, Y. Ji, and L. Wolf, "Leveraging RF-channel fluctuation for activity recognition: Active and passive systems, continuous and RSSI-based signal features," in *Proc. Int. Conf. Adv. Mobile Comput. Multimedia*. New York, NY, USA: Association for Computing Machinery, 2013, pp. 43–52.

[21] J. Liu, Y. Wang, Y. Chen, J. Yang, X. Chen, and J. Cheng, "Tracking vital signs during sleep leveraging off-the-shelf WiFi," in *Proc. 16th ACM Int. Symp. Mobile Ad Hoc Netw. Comput.* New York, NY, USA: Association for Computing Machinery, Jun. 2015, pp. 267–276.

[22] C. Chen, Y. Chen, H.-Q. Lai, Y. Han, and K. J. R. Liu, "High accuracy indoor localization: A WiFi-based approach," in *Proc. IEEE Int. Conf. Acoust., Speech Signal Process. (ICASSP)*, Mar. 2016, pp. 6245–6249.

[23] C. Chen, Y. Chen, Y. Han, H.-Q. Lai, and K. J. R. Liu, "Achieving centimeter-accuracy indoor localization on WiFi platforms: A frequency hopping approach," *IEEE Internet Things J.*, vol. 4, no. 1, pp. 111–121, Feb. 2017.

[24] G. P. Blasone, F. Colone, and P. Lombardo, "Passive radar concept for automotive applications," in *Proc. IEEE Radar Conf. (RadarConf)*, Mar. 2022, pp. 1–5.

[25] A. Quirini, G. P. Blasone, F. Colone, and P. Lombardo, "A simple NULA design strategy for target detection and DoA estimation in mobile passive radar," in *Proc. Int. Conf. Radar Syst. (RADAR)*, Oct. 2022, pp. 570–575.

[26] M. Di Seglio, F. Filippini, C. Bongioanni, and F. Colone, "Human and drone surveillance via RpF-based WiFi passive radar: Experimental validation," in *Proc. 23rd Int. Radar Symp. (IRS)*, Sep. 2022, pp. 402–407.

[27] H. Sun, L. G. Chia, and S. G. Razul, "Through-wall human sensing with WiFi passive radar," *IEEE Trans. Aerosp. Electron. Syst.*, vol. 57, no. 4, pp. 2135–2148, Aug. 2021.

[28] B. Tan et al., "Wi-Fi based passive human motion sensing for in-home healthcare applications," in *Proc. IEEE 2nd World Forum Internet Things (WF-IoT)*, Dec. 2015, pp. 609–614.

[29] Q. Chen, Y. Liu, B. Tan, K. Woodbridge, and K. Chetty, "Respiration and activity detection based on passive radio sensing in home environments," *IEEE Access*, vol. 8, pp. 12426–12437, 2020.

[30] W. Li, B. Tan, and R. Piechocki, "Passive radar for opportunistic monitoring in e-Health applications," *IEEE J. Transl. Eng. Health Med.*, vol. 6, pp. 1–10, 2018.

[31] W. Li, B. Tan, and R. J. Piechocki, "Non-contact breathing detection using passive radar," in *Proc. IEEE Int. Conf. Commun. (ICC)*, May 2016, pp. 1–6.

[32] F. Colone, F. Filippini, M. D. Seglio, P. V. Brennan, R. Du, and T. X. Han, "Reference-free amplitude-based WiFi passive sensing," *IEEE Trans. Aerosp. Electron. Syst.*, vol. 59, no. 5, pp. 6432–6451, Oct. 2023.

[33] M. D. Seglio, F. Filippini, C. Bongioanni, and F. Colone, "Reference-free WiFi PHY preamble based passive radar for human sensing," in *Proc. Int. Conf. Radar Syst. (RADAR)*, Oct. 2022, pp. 119–124.

[34] J. M. Nuñez-Ortuño, J. P. González-Coma, R. N. López, F. Troncoso-Pastoriza, and M. Álvarez-Hernández, "Beamforming techniques for passive radar: An overview," *Sensors*, vol. 23, no. 7, p. 3435, Mar. 2023.

[35] Y.-C. Lai, C.-C. Chou, M.-C. Tang, T.-S. Horng, and F.-K. Wang, "Finger gesture sensing and recognition using a Wi-Fi-based passive radar," in *IEEE MTT-S Int. Microw. Symp. Dig.*, Jun. 2019, pp. 293–296.

[36] M.-C. Tang, F.-K. Wang, and T.-S. Horng, "Vital-sign detection based on a passive WiFi radar," in *IEEE MTT-S Int. Microw. Symp. Dig.*, Sep. 2015, pp. 74–75.

[37] M.-C. Tang, F.-K. Wang, and T.-S. Horng, "Human gesture sensor using ambient wireless signals based on passive radar technology," in *IEEE MTT-S Int. Microw. Symp. Dig.*, May 2015, pp. 1–4.

[38] D. V. Q. Rodrigues and C. Li, "A microwave passive topology based on simultaneous injection-locking and injection-pulling for passive indoor sensing applications," in *Proc. Int. Microw. Antenna Symp. (IMAS)*, Feb. 2023, pp. 107–110.

[39] D. V. Q. Rodrigues, D. Tang, and C. Li, "A novel microwave architecture for passive sensing applications," in *Proc. IEEE Radio Wireless Symp. (RWS)*, Jan. 2022, pp. 57–59.

[40] D. Tang, V. G. R. Varela, D. V. Q. Rodrigues, D. Rodriguez, and C. Li, "A Wi-Fi frequency band passive biomedical Doppler radar sensor," *IEEE Trans. Microw. Theory Techn.*, vol. 71, no. 1, pp. 93–101, Jan. 2023.

[41] A. B. Carman and C. Li, "Passive multistatic wireless sensing based on discrete LNA/Mixer co-optimization and fast-startup baseband amplifier," in *Proc. IEEE Topical Conf. Wireless Sensors Sensor Netw.*, Jan. 2023, pp. 43–45.

[42] A. B. Carman and C. Li, "A digital beamforming approach for indoor passive sensing," in *Proc. IEEE Top. Conf. Wireless Sensors Sensor Netw.*, Jan. 2024, pp. 12–14.

[43] C. Feng et al., "Multitarget vital signs measurement with chest motion imaging based on MIMO radar," *IEEE Trans. Microw. Theory Techn.*, vol. 69, no. 11, pp. 4735–4747, Nov. 2021.

[44] A. B. Carman and C. Li, "Null/optimum point optimization for indoor passive radar motion sensing," in *Proc. IEEE Radar Conf. (RadarConf)*, San Antonio, TX, USA, May 2023, pp. 1–5.

[45] S. P. Hehenberger, A. Yarovoy, and A. Stelzer, "A 77-GHz FMCW MIMO radar employing a non-uniform 2D antenna array and substrate integrated waveguides," in *IEEE MTT-S Int. Microw. Symp. Dig.*, Nov. 2020, pp. 1–4.

[46] Z. Peng and C. Li, "A portable K-band 3-D MIMO radar with nonuniformly spaced array for short-range localization," *IEEE Trans. Microw. Theory Techn.*, vol. 66, no. 11, pp. 5075–5086, Nov. 2018.

[47] Y. Yang, C. Gu, R. Gale, J. Chen, and C. Li, "DC-coupled Doppler radar sensor with software-configured fine-tuning architectures for precise monitoring of complex motion patterns," in *Proc. WAMICON IEEE Wireless Microw. Technol. Conf.*, Apr. 2012, pp. 1–6.

[48] D. Tang, J. Wang, Z. Peng, Y.-C. Chiang, and C. Li, "A DC-coupled biomedical radar sensor with analog DC offset calibration circuit," in *Proc. IEEE Int. Instrum. Meas. Technol. Conf. (IMTC)*, May 2018, pp. 1–6.

[49] A. B. Carman and C. Li, "Low-cost fast-start amplifier architecture for AC-coupled measurement of low-frequency signals," *IEEE Sensors Lett.*, vol. 8, no. 5, pp. 1–4, May 2024.

Aaron B. Carman (Graduate Student Member, IEEE) received the B.S. degree in electrical engineering from Texas Tech University, Lubbock, TX, USA, in 2020, where he is currently pursuing the Ph.D. degree.

He worked as a Student Engineer with the Defense and Intelligence Solutions Division, Southwest Research Institute, San Antonio, TX, USA, in 2019. He has been working as a Research Assistant with Texas Tech University, since 2018. His current research interests include passive microwave sensors, radar system design, and RF signal modeling.

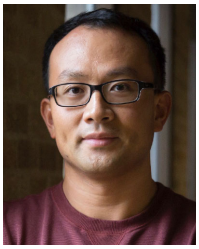

Changzhi Li (Fellow, IEEE) received the B.S. degree in electrical engineering from Zhejiang University, Hangzhou, China, in 2004, and the Ph.D. degree in electrical engineering from the University of Florida, Gainesville, FL, USA, in 2009.

He is currently a Professor with Texas Tech University, Lubbock, TX, USA. His research interests include biomedical applications of microwave technology, wireless sensors, and RF/analog circuits.

Dr. Li is a Fellow of the National Academy of Inventors (NAI). He is a Distinguished Microwave Lecturer of the IEEE Microwave Theory and Techniques Society (MTT-S), in the Tatsuo Itoh Class of 2022–2024. He is currently an Associate Editor of IEEE JOURNAL OF ELECTROMAGNETICS, RF AND MICROWAVES IN MEDICINE AND BIOLOGY. He was a recipient of the IEEE MTT-S Outstanding Young Engineer Award, the IEEE Sensors Council Early Career Technical Achievement Award, the ASEE Frederick Emmons Terman Award, and the IEEE-HKN Outstanding Young Professional Award.